Structure of the (110) $LnScO_3$ (Ln = Gd, Tb, Dy) surfaces

Zachary R. Mansley,[1] Christopher A. Mizzi,[1] Pratik Koirala,[1] Jianguo Wen,[2] and Laurence D. Marks[1,*]

[1]*Department of Materials Science and Engineering, Northwestern University, Evanston, Illinois 60208, USA*

[2]*Center for Nanoscale Materials, 9700 S. Cass Ave., Argonne National Laboratory, Lemont, Illinois 60439, USA*

(Received 20 December 2019; revised manuscript received 14 February 2020; accepted 13 March 2020; published 27 April 2020)

The surface reconstruction on the (110) surface of $LnScO_3$ (Ln = Gd, Tb, Dy) has been investigated using x-ray photoelectron spectroscopy, atomic force microscopy, and transmission electron diffraction coupled with higher-level density-functional theory methods. The experimental techniques generate constraints on the surface chemistry and structure that are used to inform the theoretical comparison of a number of potential surface structures. The resulting structure is then compared to experimental aberration-corrected transmission electron microscopy results using multislice simulation. The surfaces of both single-crystalline substrates and hydrosauna synthesized nanoparticles exhibit a Sc-rich double layer with a Sc_3O_4 termination.

DOI: 10.1103/PhysRevMaterials.4.045003

I. INTRODUCTION

Due to their high dielectric constants [1], large optical band gaps [2], abnormally large flexoelectric coefficients [3], and a recent method to produce nanoparticles with a relatively high degree of shape control [4] there has been a significant interest in studying the lanthanide (Ln) scandates, $LnScO_3$, for applications including film growth [5] and catalysis. The ability to vary the lattice parameter of the material as one moves down the lanthanide series is of interest for systematic studies, such as exploring epitaxial strain effects [6,7]. However, oxide surfaces are known to reconstruct into low-energy configurations that can differ from the bulk, and these reconstructions can have a notable impact on properties. For instance, surface reconstructions can change surface electronic states, and those with a different periodicity than the bulk lattice will have an impact on epitaxy [8–10]. In addition, surface reconstructions can change the surface chemistry, which will affect properties such as surface mobility of adsorbed species [11]. These effects are magnified for oxide nanoparticles, as the surface to bulk ratio is much larger and the surface contribution to the properties is palpable. An example of this is catalysis, where different surface properties of nanoparticles can lead to different adsorption behaviors or, in the case of supported catalysts, unexpected catalyst-support interactions [11–13].

Structurally, most members of the $LnScO_3$ family adopt a distorted orthorhombic perovskite structure (space group *Pbnm*) with a pseudocubic sublattice in the ⟨110⟩ and ⟨001⟩ directions. The pseudocubic lattice parameters relevant to this work range from 3.946 Å for $DyScO_3$ to 3.970 Å for $GdScO_3$ [6]. The ScO_6 octahedral units are rotated in phase about the [001] axis and out of phase about the [1$\bar{1}$0] axis ($a^-a^-c^+$ in Glazer notation with respect to the *Pbnm* reference frame), the rotation being more pronounced as the size of the lanthanide decreases [14].

Some literature already exists on the surface structure of these materials indicating both *A*- and *B*-site terminations, summarized by Biswas *et al.* [15]. When annealing in Ar gas a Sc-rich surface was observed via Auger electron spectroscopy [16]. A Dy-rich surface was observed after a brief (<1 h) 1320 K anneal in O_2 gas, but this was replaced by a Sc-rich surface in the same conditions at longer times (>10 h) [16]. Dirsyte *et al.* rationalize this as the oxidation, diffusion, and evaporation of Dy species under oxidizing conditions, but no structure was proposed for either surface. Additionally, a Sc-rich surface prepared using a $NaOH/H_2O$ etch was also observed and further characterized as a (1×1) structure using time of flight mass spectroscopy of recoiled ions (TOF MSRI), reflection high-energy electron diffraction (RHEED), and surface x-ray diffraction (SXRD) [17,18]. Neither the exact surface chemistry nor the atomic structure has been solved beyond hypothesizing the presence of surface oxygen vacancies [18].

Here we present theoretical and experimental evidence for the atomic structure of reconstructed $LnScO_3$ (Ln = Gd, Tb, Dy) (110) surfaces. Angle-resolved x-ray photoelectron spectroscopy (XPS) measurements and subsequent modeling indicate the surface chemistry, and a combination of transmission electron diffraction (TED) and density-functional theory (DFT) calculations shows the structure of these surfaces to be very similar regardless of the *A*-site cation. The reconstruction is also observed on nanoparticles using aberration-corrected transmission electron microscopy (TEM).

II. METHODS

Single-crystal samples of $GdScO_3$, $TbScO_3$, and $DyScO_3$ were prepared from substrates purchased through MTI Corporation. To fabricate the samples, 3-mm disks were cut from the substrates, thinned with SiC sandpaper, and dimpled using a Gatan 656 Dimple Grinder until approximately 20 um thick at the center. These dimpled samples were then ion-beam milled using a Gatan Precision Ion Polishing System between 2.5 and 5.5 keV until electron transparent. Following the ion-beam

*Corresponding author: L-marks@northwestern.edu

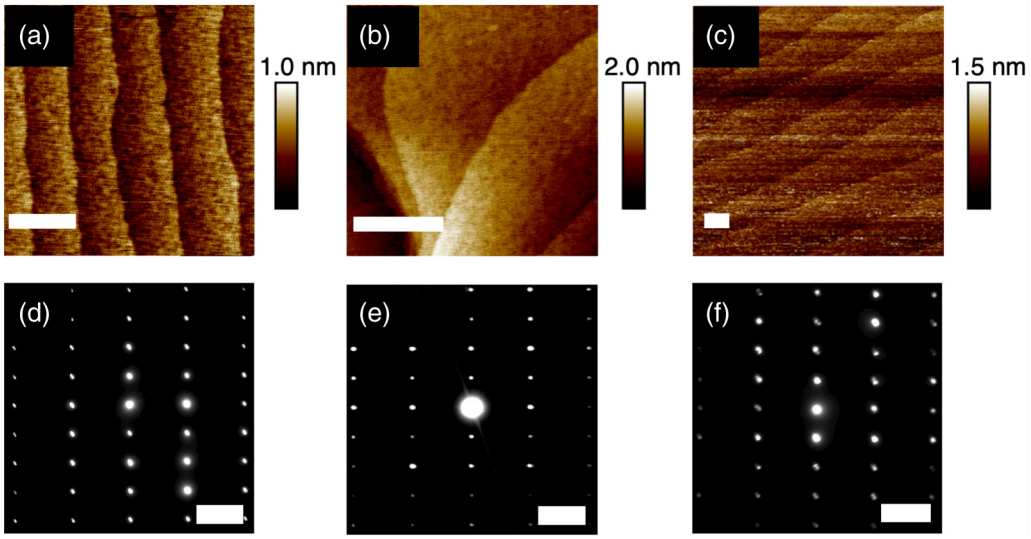

FIG. 1. Experimental data from $GdScO_3$ (a), (d), $TbScO_3$ (b), (e), and $DyScO_3$ (c), (f). AFM images (a)–(c) show clean, atomically terraced surfaces, and TED (d)–(f) along the $LnScO_3$ [110] zone axis demonstrates a lack of extra surface diffraction spots. Scale bars are 200 nm in (a)–(c) and 2 nm^{-1} in (d)–(f).

thinning, which is known to introduce surface disorder and reduce most oxide surfaces, the samples were annealed at 1050 °C in air for 12 h to reorder the surface. Annealing was done immediately preceding characterization experiments to ensure a clean sample.

Angle-resolved XPS was performed using an ESCALAB 250Xi system with a monochromated Al Kα source and all spectra are averages of 5–10 scans. A flood gun was used to compensate sample charging during the experiments. Before examining the surface chemistry using angle-resolved XPS, survey, C 1s, and O 1s spectra were acquired for all samples to ensure no spurious signal from impurities or adsorbates would impact compositional analysis. In all cases these confirmed that there were no impurities above the detection limit and minimal adsorbed carbon and water. Atomic force microscopy (AFM) images were acquired with a Bruker FastScan AFM operated in tapping mode to characterize the larger-scale surface morphology.

Electron microscopy was performed at 200 kV using a Hitachi H8100 and the Argonne aberration-corrected TEM (ACAT), which is a modified FEI Titan 80-300 ST with Cs and Cc correction. The Hitachi was used for diffraction of the single-crystal samples to observe surface diffraction spots, and the ACAT was used for high-resolution profile-view imaging to directly observe the reconstruction. The profile-view imaging of the (110) surface was performed on $GdScO_3$ and $DyScO_3$ nanoparticles prepared as described by Paull *et al.* [4], tilted to either the $[\bar{1}10]$ or $[\bar{1}12]$ zones. Multislice simulations were performed using the MACTEMPAS code using typical working conditions for the ACAT (200 kV, $<$10 um Cs, 40-nm focal spread).

The all-electron augmented plane wave+local orbitals WIEN2K package was used for DFT calculations [19]. The exchange and correlation term was approximated using the PBESOL functional with on-site hybrids, which adds an exact-exchange hybrid correction within the muffin tins [20–22]. In this work, on-site hybrid fractions of 0.38, 0.50, and 0.80 were used for the Ln 4f, Ln 5d, and Sc 3d orbitals, respectively. These values are those reported in Mizzi *et al.* [23]. They correspond to the hybrid fractions that minimize the forces on the atoms using the known bulk positions [24], and were shown to yield simulated XPS valence band spectra in good agreement with experiment [23]. The Ln 4f hybrid term corrects for the known inadequacies of conventional functionals in describing the exchange coupling of 4f states; the larger terms for the d orbitals reduce the well-known overhybridization of the essentially empty metal d states with neighboring O 2p states, increasing the ionicity. A value of 6.0 was used for the plane-wave expansion parameter RKMAX, and a $1 \times 4 \times 4$ k-point mesh was used. Muffin-tin radii of 2.02, 1.82, and 1.68 atomic units were chosen for the Ln, Sc, and O atoms, respectively. These radii were chosen to minimize the inclusion of O 2p tails within the cation muffin tins which disrupts the exact-exchange corrections within the Ln and Sc muffin tins [23]. A slab with 92 unique atoms, $P121/m1$ symmetry, and approximately 14 Å of vacuum was used to model the surface [20–22]. Optimized lattice constants calculated using the on-site hybrid method with the PBESOL functional were used throughout this work. The electron density and all atomic positions were simultaneously converged using a quasi-Newton algorithm [25]. A ferromagnetic ordering was imposed on the structure; test calculations with an antiferromagnetic ordering resulted in minimal changes in positions or energy. Spin-orbit couplings were not included in this work.

III. RESULTS

AFM of the surfaces in Figs. 1(a)–1(c) confirms an atomically stepped (110) surface following the annealing as seen in similar materials [15,26]. In addition, surface-sensitive electron diffraction, which involves using an electron beam in a nanodiffraction geometry on a very thin region of the sample, was done to observe the reconstruction's periodicity. TED in plan-view shown in Figs. 1(d)–1(f) suggests a structure with

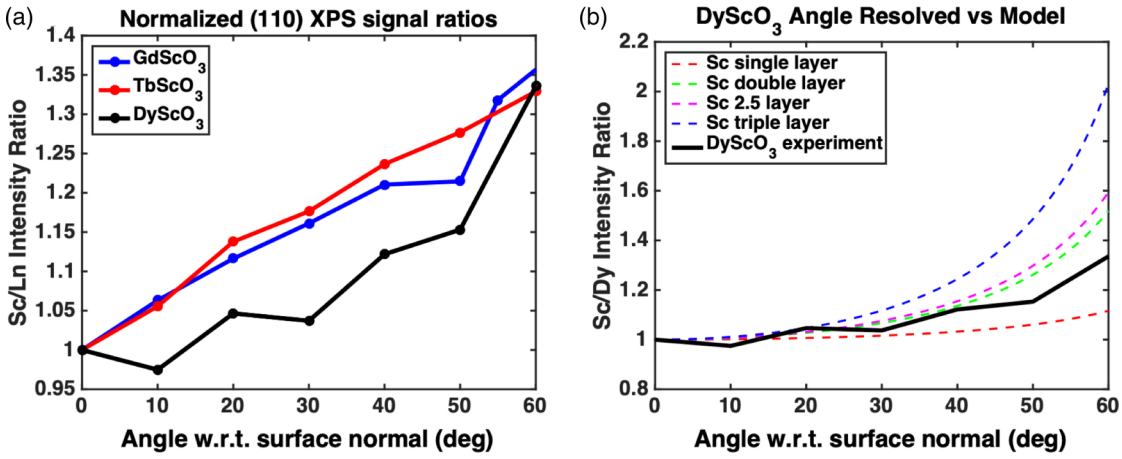

FIG. 2. (a) Experimental angle-resolved XPS intensity ratios of the integrated scandium $2p$ and the lanthanide $3d$ signals for the three $LnScO_3$ materials. Plotting the data against the model in (b) shows the experimental data have the best approximate match to a double-layer scandium termination, but the model is too crude to determine the exact chemistry.

a (1×1) periodicity with respect to the (110) surface, as no extra diffraction spots are present. We note that there was minimal diffuse scattering, which indicates that the surface has a true (1×1) periodicity rather than a disordered surface with an average (1×1) periodicity but local disorder. The latter is typical of samples prior to annealing.

Next, angle-resolved XPS was used to determine the surface chemistry. Figure 2(a) shows the ratios of the Sc $2p$ and the Ln $3d$ XPS signals as a function of angle; here normal incidence is at zero degrees. As the angle increases and the signal from the surface becomes more dominant, the Sc signal increases with respect to the Ln signal. This indicates that the surfaces of all three scandates are similarly Sc rich. It should be noted that there is a large uncertainty in these angle-resolved XPS measurements due to factors such as photoelectron channeling as well as minor variations in the in-plane orientation between experiments and the area scanned. Hence the total error is difficult to quantify. To further estimate the number of scandium layers in the surface reconstruction, the XPS signals were theoretically modeled.

The ratio of Sc $2p$ to Ln $3d$ signals from a ScO_2^--terminated bulk slab, $I_{Sc,\mathrm{bulk}}$ and $I_{Ln,\mathrm{bulk}}$ respectively, is given in Eq. (1),

$$\frac{I_{Sc2p,\mathrm{bulk}}}{I_{Ln3d,\mathrm{bulk}}} = \frac{\alpha_{Sc2p}\ \rho_{Sc}}{\alpha_{Ln3d}\ \rho_{Ln}} \frac{\sum_{m=1}^{\infty} D_{Sc2p}^{2m-2}}{\sum_{m=1}^{\infty} D_{Ln3d}^{2m-1}} = \frac{\alpha_{Sc2p}\rho_{Sc}}{\alpha_{Ln3d}\rho_{Ln}} \frac{1}{1-D_{Sc2p}^2} \frac{D_{Ln3d}}{D_{Ln3d}^2-1}, \tag{1}$$

where α_i is the photoionization cross section of the indicated orbital, ρ_j is the areal number density of atom j, m is the number of unit cells generating signal, and $D_i = \exp(-\frac{t}{\cos(\theta)\lambda_i})$ is an exponential damping function which is a function of the layer thickness t, inelastic mean-free path of the electron λ_i, and angle towards the detector θ [27–29]. Each summed term represents one unit cell, and the topmost layer of the $LnScO_3$ unit is ScO_2^-, representing a single Sc layer termination. This sum converges as shown for a slab thicker than the inelastic mean-free path of the relevant electrons in the system. The total signal intensities for different surface chemistries, I_{Sc2p} and I_{Ln3d}, can then be calculated by adding surface layer contributions to the preceding bulk intensities. This is shown in Eq. (2) below for the case of an extra Sc surface layer (resulting in a double-layer termination):

$$\frac{I_{Sc2p}}{I_{Ln3d}} = \frac{\alpha_{Sc2p}\rho_{Sc} + D_{Sc2p}I_{Sc2p,\mathrm{bulk}}}{D_{Ln3d}I_{Ln3d,\mathrm{bulk}}}. \tag{2}$$

Figure 2(b) shows how the intensity ratio varies when changing the number of surface layers and their respective chemistries. As demonstrated, changing the number of layers results in a significant change in the intensity ratio, while changing the chemistry of the terminating layer (shown as 2 and 2.5 layers), only results in minor changes. In this case, the experimental data were found to match best with a double layer of scandium oxide Sc_xO_y on the surface. As derived, the model assumes a perfectly clean surface, but in reality there will always be a small amount of adsorbates. This would affect the results by introducing a small amount of surface damping, although the magnitude would be negligible and within the previously mentioned experimental spread.

The experimental results indicate that there is no larger cell reconstruction, and that the surface was a scandium-rich double layer (with oxygen). This reduces the possible structures from a very large number to a small number. We next apply chemical constraints to further reduce the number of possibilities. Oxide surfaces are not random arrangements of atoms; there are chemical constraints such as valence neutrality and Pauling's rules by which they abide, as shown by Andersen *et al.* [30]. Briefly, three of the main constraints on oxide surface structures are (1) the structure will maximize symmetry; (2) corner-sharing polyhedra are preferred to edge sharing, which in turn are preferred to face sharing; and (3) the surface will adopt bulk-like structures if possible. Therefore, the inner layer of the double-layer scandium termination will adopt a bulk-like structure, leaving the charge balancing and rearrangement largely in the outermost layer. In this case, based upon the XPS data and valence neutrality conditions the (110) surface adopts a surface chemistry of Sc_3O_4, and these atoms will be arranged on the surface to both maximize symmetry and minimize face-sharing polyhedra while

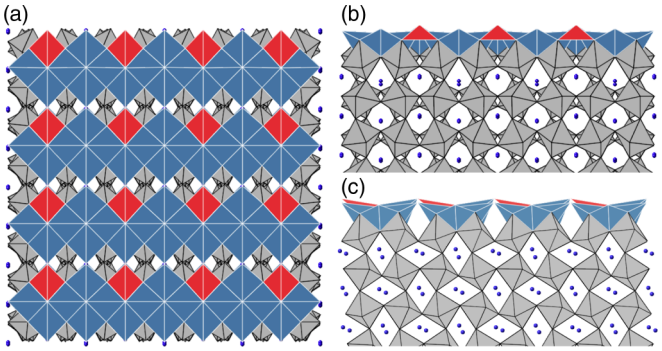

FIG. 3. DFT relaxed structure shown for $DyScO_3$. The three major pseudocubic axes are shown. With respect to the *Pbnm* structure, the view directions are [110] (a), [$\bar{1}$10] (b), [001] (c). Bulk ScO_6 octahedra are gray, surface $ScO_{5[]}$ octahedra are blue, and surface ScO_4 tetrahedra are red. Dy atoms are pictured as blue spheres.

maintaining reasonable coordinations with each other and the inner layer of the double layer. The lack of extra surface diffraction spots in the TED experiments (and minimal diffuse scattering) indicates that the periodicity of the reconstruction was the same as the bulk repeat unit in the [110] direction, further reducing the number of feasible structures.

The combination of the experimental and chemical constraints leads to a total of six occupied Sc polyhedral sites for the outermost layer out of the eight available sites. With these constraints established, DFT calculations were performed on all unique permutations using this experimental information. The lowest energy minimized structure for $DyScO_3$ is shown in Fig. 3. The overall motif (i.e., the periodicity and occupied sites) of the reconstruction is the same for $GdScO_3$, with minor variations in the exact positions of the surface atoms. This is not surprising as the materials have different lattice parameters and octahedral tilts below the reconstructed surface. We do not suggest an exact structure for $TbScO_3$ here because there are ambiguities about the exact position of the single minority 4f electron as discussed previously [23]. However, we do suggest that it reconstructs in a similar fashion based on the experimental evidence from AFM, TED, and XPS. Full atomic positions for the (110) surfaces of $GdScO_3$ and $DyScO_3$ are provided in Supplemental CIF files [31].

To experimentally verify the low-energy structure predicted from theory, high-resolution TEM profile-view imaging of the $GdScO_3$ nanoparticle surface was compared to multislice simulations of the images based on the predicted structure. As shown in Fig. 4, a good match is observed. High-resolution TEM profile-view imaging of the $DyScO_3$ nanoparticle surface is also consistent with a double-layer termination.

Having experimentally confirmed the predicted atomic structure of the $DyScO_3$ and $GdScO_3$ reconstructions, we now analyze deviations from the bulk electronic structure arising from the Sc-rich surfaces using our DFT calculations. We emphasize changes to the valence band and the creation of in-gap surface Sc 3d and O 2p states because both are important in the context of thin-film heterostructures, a common use for $DyScO_3$ and $GdScO_3$. *Ln* 4f states, although included in this analysis for completeness, are shown to be essentially bulklike throughout the slab and their valence band contributions have been analyzed in detail elsewhere [23].

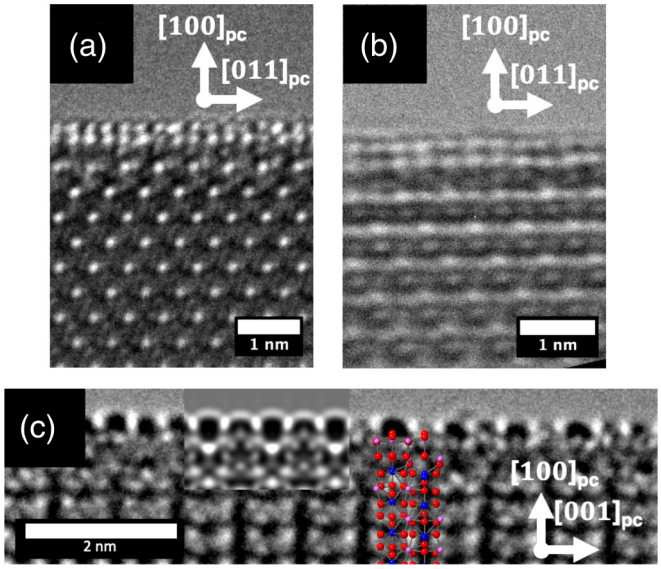

FIG. 4. High resolution electron microscopy (HREM) profile-view imaging along the psuedocubic (0$\bar{1}$1) zone axis for $GdScO_3$ (a) and $DyScO_3$ (b) showing a double-layer termination. The $DyScO_3$ particles exhibited significant charging and mobility under the electron beam, leading to substantial drifting. Imaging along the pseudocubic (010) zone axis of $GdScO_3$ along with overlaid multislice simulation and solved crystal structure are shown in (c).

Figure 5 compares the Sc 3d and O 2p partial density of states (pDOS) in the three Sc-O coordination environments in these $GdScO_3$ and $DyScO_3$ slabs: ScO_6 octahedra, $ScO_{5[]}$

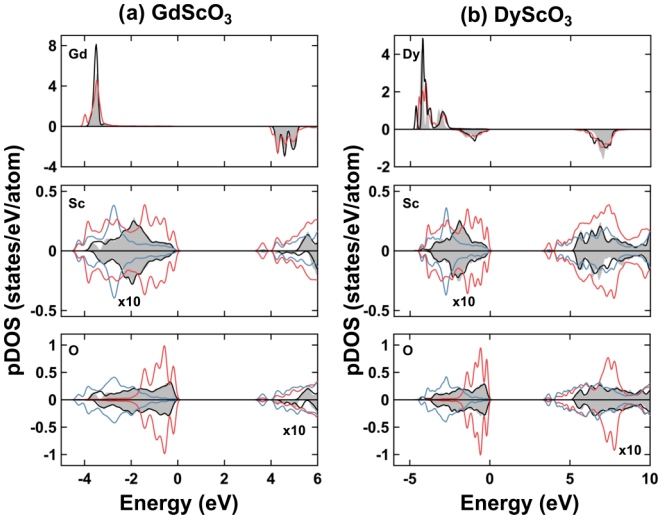

FIG. 5. Partial density of states associated with *Ln* 4f, Sc 3d, and O 2p states in (a) $GdScO_3$ and (b) $DyScO_3$. Positive and negative DOS values are spin up and down, respectively. Negative energies correspond to occupied states and positive energies correspond to unoccupied states, with zero set to the bulk valence band maximum. In all cases states from the central-most layer of the surface slabs (black, solid lines) are compared to states from separate bulk calculations (black, shaded). While the *Ln* has only one surface-most unit (technically the second subsurface layer, plotted in red), the Sc and O have two unique polyhedral surface structures: $ScO_{5[]}$ (blue), and ScO_4 (red). The occupied Sc and unoccupied O states have been scaled by a factor of 10 for clarity as indicated in the plots.

surface octahedra with a missing oxygen, and ScO_4 surface tetrahedra. The valence band is dominated by filled O $2p$ and Ln $4f$ states, and the conduction band by unoccupied Sc $3d$ states. In both materials, the pDOS associated with the ScO_6 octahedra taken from the central-most slab layer are nearly indistinguishable from independent bulk calculations, and below the double layer the Sc $3d$ and O $2p$ pDOS only exhibit minor deviations from the bulk pDOS. This indicates sufficiently large slabs were used in the simulations. In contrast there are sizable differences between the Sc $3d$ and O $2p$ states in the surface double layer and the bulk in both materials: states associated with ScO_4 are concentrated near the valence band maximum whereas those associated with $ScO_{5[]}$ are concentrated near the valence band minimum. Additionally, our calculations indicate that $GdScO_3$ and $DyScO_3$ possess in-gap surface states located 4–5 eV above the valence band maximum which are mostly Sc $3d$ in character and primarily associated with ScO_4 tetrahedra on the surface. These changes in the surface electronic structure and the presence of in-gap surface states, which have been experimentally confirmed in $DyScO_3$ using electron energy-loss spectroscopy and ultraviolet photoelectron spectroscopy, likely play a role in the large charging observed in lanthanide scandates [3,32]. These surface states have yet to be experimentally confirmed in $GdScO_3$.

IV. DISCUSSION

The {100} pseudocubic atomic planes of 332 ABO_3 perovskite materials in the *Pbnm* structure [which are the (110), $(\bar{1}10)$, and (001)] are either BO_2^- or AO^+, with minor differences in the relative directions of the octahedral tilts as indicated by the Glazer notation description in the Introduction. In light of the valence neutrality constraint of the surface, this nonzero valence of each layer implies that the surface terminations cannot exist as bulk truncations and must undergo reconstruction, adsorption of a foreign species, or a similar process to be valence neutral. For example, each pseudocubic unit of the double-layer reconstruction reported here possesses a +0.5 valence to match the negatively valent BO_2^- layer below. Besides valence neutrality, surface structures must adhere to Pauling's rules; the reconstruction reported here is the lowest-energy solution to simultaneously neutralize the valence while satisfying Pauling's rules. Importantly, satisfying these two constraints for {100} pseudocubic surfaces of 332 perovskites is agnostic to many details of the material: the valence of each layer and the structural units are common to all {100} pseudocubic surfaces of 332 perovskites. Therefore, it is reasonable to suspect this double-layer surface reconstruction will lie on the convex hull for most if not all {100} pseudocubic surfaces of 332 perovskites. This is supported by our observations on these three scandates where we have found evidence for the same surface reconstruction independent of the A-site cation.

This should not be taken to indicate that this Sc-rich double-layer reconstruction is the only possible surface structure for these systems. This is determined by the balance between exchange of atoms between the bulk and the initial surface composition whether from epi-polishing, a buffered solution or similar treatment, or deposition onto the surface. For instance, it is established that extended annealing of strontium titanate in oxidizing conditions leads to strontium vacancies in the bulk which diffuse to the surface, leading to a strontium oxide-rich surface [33,34]. In contrast, aqueous treatments preferentially remove strontium from the surface leaving titanium-rich surfaces; titanium-rich surfaces are also produced following annealing in reducing conditions or ion-beam milling [26,33]. Our results imply similar B-site enrichment for the $LnScO_3$ family, although more work is required to fully define the details, both the surface composition as a function of (pre)treatment as well as the relevant bulk point defects.

ACKNOWLEDGMENTS

The authors thank R. J. Paull for synthesizing and providing faceted nanoparticle samples for imaging. This research was funded by the Northwestern University Institute for Catalysis in Energy Processes (ICEP) with Grant No. DOE DE-FG02-03-ER 15457 (Z.R.M.), and U.S. Department of Energy, Office of Science, Basic Energy Sciences, under Award No. DE-FG02-01ER45945 (C.A.M., P.K.). We also acknowledge the Center for Nanoscale Materials, and Office of Science user facility which was supported by the U.S. Department of Energy, Office of Science, Office of Basic Energy Sciences, under Contract No. DE-AC02-06CH11357.

[1] C. Zhao, T. Witters, B. Brijs, H. Bender, O. Richard, M. Caymax, T. Heeg, J. Schubert, V. V. Afanas'ev, A. Stesmans, and D. G. Schlom, Appl. Phys. Lett. **86**, 132903 (2005).

[2] D. G. Schlom and J. H. Haeni, MRS Bull. **27**, 198 (2002).

[3] P. Koirala, C. A. Mizzi, and L. D. Marks, Nano Lett. **18**, 3850 (2018).

[4] R. J. Paull, Z. R. Mansley, T. Ly, L. D. Marks, and K. R. Poeppelmeier, Inorg. Chem. **57**, 4104 (2018).

[5] J. H. Haeni, P. Irvin, W. Chang, R. Uecker, P. Reiche, Y. L. Li, S. Choudhury, W. Tian, M. E. Hawley, B. Craigo, A. K. Tagantsev, X. Q. Pan, S. K. Streiffer, L. Q. Chen, S. W. Kirchoefer, J. Levy, and D. G. Schlom, Nature (London) **430**, 758 (2004).

[6] R. Uecker, B. Velickov, D. Klimm, R. Bertram, M. Bernhagen, M. Rabe, M. Albrecht, R. Fornari, and D. G. Schlom, J. Cryst. Growth **310**, 2649 (2008).

[7] J. A. Enterkin, R. M. Kennedy, J. Lu, J. W. Elam, R. E. Cook, L. D. Marks, P. C. Stair, C. L. Marshall, and K. R. Poeppelmeier, Top. Catal. **56**, 1829 (2013).

[8] X. Zhu, M. D. Morales-Acosta, J. Shen, F. J. Walker, J. J. Cha, and E. I. Altman, Phys. Rev. B **92**, 165414 (2015).

[9] S. Akbulut, A. Akbulut, M. Ozdemir, and F. Yildiz, J. Magn. Magn. Mater. **373**, 155 (2015).

[10] E. M. Kneedler, B. T. Jonker, P. M. Thibado, R. J. Wagner, B. V. Shanabrook, and L. J. Whitman, Phys. Rev. B **56**, 8163 (1997).

[11] B. R. Chen, L. A. Crosby, C. George, R. M. Kennedy, N. M. Schweitzer, J. G. Wen, R. P. Van Duyne, P. C. Stair, K. R. Poeppelmeier, L. D. Marks, and M. J. Bedzyk, ACS Catal. **8**, 4751 (2018).
[12] G. A. Somorjai, Annu. Rev. Phys. Chem. **45**, 721 (1994).
[13] F. Polo-Garzon, V. Fung, X. M. Liu, Z. D. Hood, E. E. Bickel, L. Bai, H. J. Tian, G. S. Foo, M. F. Chi, D. E. Jiang, and Z. L. Wu, ACS Catal. **8**, 10306 (2018).
[14] A. M. Glazer, Acta Crystallogr. B **28**, 3384 (1972).
[15] A. Biswas, C. H. Yang, R. Ramesh, and M. H. Jeong, Prog. Surf. Sci. **92**, 117 (2017).
[16] R. Dirsyte, J. Schwarzkopf, G. Wagner, R. Fornari, J. Lienemann, M. Busch, and H. Winter, Surf. Sci. **604**, L55 (2010).
[17] J. E. Kleibeuker, G. Koster, W. Siemons, D. Dubbink, B. Kuiper, J. L. Blok, C. H. Yang, J. Ravichandran, R. Ramesh, J. E. ten Elshof, D. H. A. Blank, and G. Rijnders, Adv. Funct. Mater. **20**, 3490 (2010).
[18] J. E. Kleibeuker, B. Kuiper, S. Harkema, D. H. A. Blank, G. Koster, G. Rijnders, P. Tinnemans, E. Vlieg, P. B. Rossen, W. Siemons, G. Portale, J. Ravichandran, J. M. Szepieniec, and R. Ramesh, Phys. Rev. B **85**, 165413 (2012).
[19] P. Blaha, K. Schwarz, G. Madsen, D. Kvasnicka, J. Luitz, R. Laskowski, F. Tran, and L. D. Marks, WIEN2K, *An Augmented Plane Wave+ Local Orbitals Program for Calculating Crystal Properties* (Technical University of Wien, Austria, 2001).
[20] F. Tran, J. Kunes, P. Novak, P. Blaha, L. D. Marks, and K. Schwarz, Comput. Phys. Commun. **179**, 784 (2008).
[21] P. Novak, J. Kunes, L. Chaput, and W. E. Pickett, Phys. Status Solidi B **243**, 563 (2006).
[22] J. P. Perdew, A. Ruzsinszky, G. I. Csonka, O. A. Vydrov, G. E. Scuseria, L. A. Constantin, X. Zhou, and K. Burke, Phys. Rev. Lett. **100**, 136406 (2008).
[23] C. A. Mizzi, P. Koirala, and L. D. Marks, Phys. Rev. Mater. **2**, 025001 (2018).
[24] M. Schmidbauer, A. Kwasniewski, and J. Schwarzkopf, Acta Cryst. Sect. B-Struct. Sci. Cryst. Eng. Mater. **68**, 8 (2012).
[25] L. D. Marks, J. Chem. Theory Comput. **9**, 2786 (2013).
[26] M. Kawasaki, K. Takahashi, T. Maeda, R. Tsuchiya, M. Shinohara, O. Ishiyama, T. Yonezawa, M. Yoshimoto, and H. Koinuma, Science **266**, 1540 (1994).
[27] E. McCafferty and J. P. Wightman, Appl. Surf. Sci. **143**, 92 (1999).
[28] C. S. Fadley, R. J. Baird, W. Siekhaus, T. Novakov, and S. A. Bergstrom, J. Electron Spectrosc. Relat. Phenom. **4**, 93 (1974).
[29] T. A. Carlson and G. E. McGuire, J. Electron Spectrosc. Relat. Phenom. **1**, 161 (1972).
[30] T. K. Andersen, D. D. Fong, and L. D. Marks, Surf. Sci. Rep. **73**, 213 (2018).
[31] See Supplemental Material at http://link.aps.org/supplemental/10.1103/PhysRevMaterials.4.045003 for CIFs of the DFT relaxed surface structures.
[32] C. A. Mizzi, P. Koirala, A. Gulec, and L. D. Marks, Ultramicroscopy **203**, 119 (2019).
[33] Y. Lin, Ph.D. thesis, Northwestern University, 2014.
[34] A. G. Schrott, J. A. Misewich, M. Copel, D. W. Abraham, and Y. Zhang, Appl. Phys. Lett. **79**, 1786 (2001).